The Astrophysical Journal, 994:182 (9pp), 2025 December 1 https://doi.org/10.3847/1538-4357/ae1a47

Near-Sun Characteristics of a CME Inferred from Observations in the 5303 Å Coronal Emission Line

V. Muthu Priyal[1], R. Ramesh[1], Jagdev Singh[1], K. Sasikumar Raja[1], and N. Gopalswamy[2]
[1] Indian Institute of Astrophysics, Koramangala 2nd Block, Bangalore 560034, Karnataka, India
[2] NASA Goddard Space Flight Center, Greenbelt, MD, USA
Received 2025 July 18; revised 2025 October 16; accepted 2025 October 24; published 2025 November 25

Abstract

Using observations of the solar corona in the 5303 Å (Fe XIV) emission line with the Visible Emission Line Coronagraph (VELC) on board Aditya-L1, we estimated the electron density (N_e), thermal energy ($E_{\rm CME}$), and mass ($M_{\rm CME}$) of a coronal mass ejection (CME) very close to the Sun at heliocentric distance $r \approx 1.06R_\odot$. The corresponding values are $N_e \approx 3.7 \times 10^8$ cm^{-3}, $E_{\rm CME} \approx 9.4 \times 10^{28}$ erg, and $M_{\rm CME} \approx 2.7 \times 10^{14}$ g, respectively. The procedure adopted suggests a possibility to understand the properties of the CMEs in the visible wavelength range, particularly during the temporal phase close to their onset. The widths and Doppler velocities of the line are nearly constant in the VELC field of view (FoV $\approx$ 1.06–1.50$R_\odot$). The values are $\approx$0.85 Å and $\approx$+2 km s^{-1}, respectively.

Unified Astronomy Thesaurus concepts: The Sun (1693); Solar corona (1483); Solar coronal lines (2038); Solar coronal mass ejections (310); Solar activity (1475); Spectroscopy (1558)

1. Introduction

Dynamic phenomenon in the solar atmosphere like flares and coronal mass ejections (CMEs) are driven by the sudden release of magnetically stored energy. Among the two, CMEs are large-scale eruptions of plasma and magnetic fields from the Sun that significantly influence space weather by triggering geomagnetic storms that can disrupt both spaceborne and ground-based technological systems. The CME has the largest fraction of the released energy during the occurrence of energetic events (A. G. Emslie et al. 2005). Understanding the energetics of CMEs is crucial for modeling their propagation and impact on the heliosphere. The amount of energy required to disrupt initially closed magnetic field lines and to lift and accelerate CMEs is a key ingredient of CME initiation models. Observations with the Large Angle and Spectrometric Coronagraphs (LASCO) C2 and C3 (G. E. Brueckner et al. 1995) on board the Solar and Heliospheric Observatory (SOHO) continue to provide valuable data on the potential and kinetic energy of the CMEs in the distance range $r \approx$ 3–30$R_\odot$ (A. Vourlidas et al. 2000). The near-Sun corona ($r \lesssim 1.5R_\odot$) governs the early acceleration and kinematics of CMEs. However, the evolution of CMEs in this region remains less understood due to the lack of continuous observations. Detailed spectroscopic and imaging studies are essential to determine their dynamic evolution during the initial phase of propagation (E. Landi et al. 2010; H. Tian et al. 2013; B. Boe et al. 2020). There are indications that the thermal energy input into CMEs is comparable to the kinetic energy of the ejected plasma (A. Akmal et al. 2001; A. Ciaravella et al. 2001; N. A. Murphy et al. 2011) from observations made at different distances in the range $r \approx$ 1.7–3.5$R_\odot$ with the Ultraviolet Coronagraph Spectrometer (UVCS; J. L. Kohl et al. 1995) on board SOHO. According to A. Kumar & D. M. Rust (1996), an expanding flux rope structure (CME) transforms magnetic energy into kinetic energy and plasma heating, almost equally. The mass and kinetic energy of CME plasma can be estimated from white light coronagraph images, but the thermal energy is more difficult to determine (A. Bemporad 2022). The thermal state of a CME evolves as it propagates through the corona. CMEs often expand as they travel outward from the Sun. For ideal adiabatic expansion, the CMEs should cool. The heating processes occurring during the CME expansion can slow the cooling rate, and the plasma temperature can remain nearly constant (J. Sheoran et al. 2023). Several heating mechanisms for individual events are reported (A. Bemporad et al. 2007; J.-Y. Lee et al. 2009; E. Landi et al. 2010; N. A. Murphy et al. 2011). A statistical study using near-Sun observations can help to address the issue. Further, quantifying CME heating would be useful to assess how the total magnetic energy released is converted into kinetic, potential, thermal, and nonthermal components. Knowing the partitioning of energy among these forms is a necessary step to understand the physical processes involved (A. Akmal et al. 2001; A. Ciaravella et al. 2001; A. G. Emslie et al. 2005; P. Subramanian & A. Vourlidas 2007; J.-Y. Lee et al. 2009; N. A. Murphy et al. 2011). A knowledge of plasma temperature and density within the CMEs is important to understand these processes. In the corona, the ratio of line to continuum becomes flat (fixed) beyond a certain height where the ions become frozen in their charge state. The ion charge can no longer change. The ionization state observed in the interplanetary medium is a direct indication of the temperature of the corona (A. J. Hundhausen et al. 1968). The evolution of electron density, temperature, etc. with distance in the corona can be used to infer the frozen-in charge states (E. Landi et al. 2012; S. R. Habbal et al. 2013). The Visible Emission Line Coronagraph (VELC) on board Aditya-L1 provides continuous high-resolution spectroscopic observations of the solar corona, allowing detailed investigations of CME dynamics comparatively closer to the solar limb. Using spectroscopic observations with VELC in the Fe XIV (5303 Å) green line, the

brightest of all solar coronal emission lines in the visible spectral range, we show that it is feasible to estimate the thermal energy input to a CME, as well as its density and mass. In this study, we report the values of these parameters for a CME event observed by VELC near the solar limb at $r \approx 1.06R_{\odot}$.

2. Observations and Data Analysis

The VELC payload on board ADITYA-L1 is an internally occulted solar coronagraph with capability to carry out multislit spectroscopic observations using four straight slits, thereby making it possible for four different regions of the solar corona to be observed simultaneously (R. Ramesh et al. 2024; J. Singh et al. 2025). The radius of the occulter is $1.05R_{\odot}$. The length of each slit is along the north–south direction of Sun, and the width (dispersion) is along the east–west direction of Sun. The field of view (FoV) covered by the slit length is $\pm 1.5R_{\odot}$. The slit width is 50 μm. Typically, the first and fourth slits are used to observe the corona above the east and west limbs of the Sun, respectively. The coronal regions above the north and south limbs of the Sun are observed using the second and third slits together. There are two observational modes in VELC: "sit-stare" and "raster scan." The sit-stare mode observes the solar corona at a fixed position for a chosen time and interval, while the raster mode scans the solar corona from -1.5 to $+1.5R_{\odot}$ (from east to west of the solar limb). The scan range for each slit is $0.75R_{\odot}$ (-1.5 to $-0.75R_{\odot}$ for slit 1, -0.75 to $0R_{\odot}$ for slit 2, 0 to $0.75R_{\odot}$ for slit 3, and 0.75 to $1.5R_{\odot}$ for slit 4). The spatial resolution and spectral dispersion of the spectra observed in the 5303 Å line are $1\farcs25$ per pixel and 0.0284 Å per pixel, respectively. The pixel size is 6.5 μm. In raster scan mode, the image from -1.5 to $+1.5R_{\odot}$ is scanned using a "linear scan mechanism" (LSM; J. Singh et al. 2025). When the LSM moves by 20 μm, the image on each of the four slits shift simultaneously by 40 μm ($\approx 7\farcs7$ in the image plane). Since the slit width is 50 μm ($\approx 9\farcs6$ in the image plane), there will be an overlap of $\approx 1\farcs9$ between the coronal data obtained from successive LSM positions. In this manner, the LSM moves in the chosen step interval, and the entire coronal image is scanned. For the step size mentioned above, 95 steps will be required to observe the corona from -1.5 to $+1.5R_{\odot}$. The sparse raster limits the spatial resolution in the east–west direction. We averaged data from 4 pixels along the slits to have comparable resolution in the north–south direction also. So, the effective resolution along the spatial direction of the slit is $5''$. Note that there can be superposition of different coronal features along the line of sight (LoS) since the FWHM of the 5303 Å filter used in VELC is ≈ 7 Å (see, e.g., A. Bemporad et al. 2017). By stacking the emission line parameters measured from the observed spectra at different spatial positions, two-dimensional coronal maps of emission intensity, emission line width, and Doppler velocity are generated. The methodology used to extract the emission line parameters is described in V. Muthu Priyal et al. (2024, 2025) and J. Singh et al. (2025). The data reduction procedure involves (i) preprocessing of raw spectra, including dark subtraction, flat-field correction, and scattered light correction; (ii) Gaussian fitting to the observed emission lines for extracting parameters such as peak intensity, Doppler velocity, and emission line width; and (iii) correction for instrumental broadening using the known instrumental width (0.213 Å) and the equivalent width of the 5302.3 Å photospheric absorption line (0.157 Å). UVCS observations of CMEs in O VI indicate the need for two Gaussians, broad and narrow, to get a good fit (S. Mancuso et al. 2002), but we approximated the line profiles by a single Gaussian function due to scattering related signal-to-noise ratio (SNR) issues in the VELC observations (J. Singh et al. 2025). The presence of any additional blue- or redshifted emission, other than that inferred from the Doppler shift in the wavelength of the peak line intensity, can be missed because of this.

For the present study, spectroscopic observations in the Fe XIV (5303 Å) emission line in the raster scan mode using VELC on 2024 September 13 (00:30–01:50 UT) are used. The exposure time for each frame is 4 s, with $1\times$ detector gain and 20 s interval between successive raster steps. At each step, five frames were acquired and binned to save as a single frame on board to improve the SNR. The onboard binning helps to reduce the data volume also. The raster scan was performed by scanning the coronal image from -1.5 to $+1.5R_{\odot}$ in 95 steps, with a chosen step size of 20 μm. The total time taken for one raster scan with the above step interval is $\approx$35 minutes. Following the data reduction procedure described above, we generated raster scan maps of emission line intensity, line width, and Doppler velocity by stacking the computed parameters from 95 spectra. The raster scan images generated using emission line intensity corresponding to slit 4 during the periods 00:30–01:05 UT and 01:15–01:50 UT are shown in Figures 1(a) and (c), respectively. The horizontal and vertical discontinuities seen in the images are due to residuals that remain even after flat-fielding and correcting for satellite pointing issues. The details related to the latter provided by the SPICE data (satellite attitude parameters) do not fully capture the jitter and pointing instabilities. The reasons for this are unclear at present. Scattering is another cause for concern. Regarding the "flat," we do not have provision to generate it in orbit, as in SOHO/LASCO-C1.[3] We correct for the discontinuities by considering the average and minimum background corona over a nearly one month observing period centered around the date of observation.

A comparison of the coronal region enclosed within the boxes in Figures 1(a) and (c) indicate that the bright structure present inside the box in Figure 1(a) has changed and dimmed to a large extent in Figure 1(c). The presence and absence of the abovementioned structure can be seen more clearly in Figures 1(b) and (d), contour versions of Figures 1(a) and (c), respectively. These observations suggest that the coronal plasma associated with the structure was ejected from the Sun after the end-time of the raster scan observations shown in Figure 1(a), i.e., 01:05 UT, and before the start time of the raster scan observations shown in Figure 1(c), i.e., 01:15 UT. The structure corresponds to active region AR13811 at the heliographic location S13W87 on 2024 September 13, associated with a CME observed in white light with SOHO/LASCO, and an M1.5 class soft X-ray flare observed with the Geostationary Operational Environmental Satellite on that day. The flare period is 00:46–01:05 UT, with peak at 00:56 UT.[4] From the SOHO/LASCO CME catalog,[5] we find that the mean position angle of the CME is $\approx 260^{\circ}$. This is in close agreement with the position angle of the bright structure seen

[3] https://lasco-www.nrl.navy.mil/index.php?p=content/handbook/hndbk_4
[4] https://www.solarmonitor.org/
[5] https://cdaw.gsfc.nasa.gov/

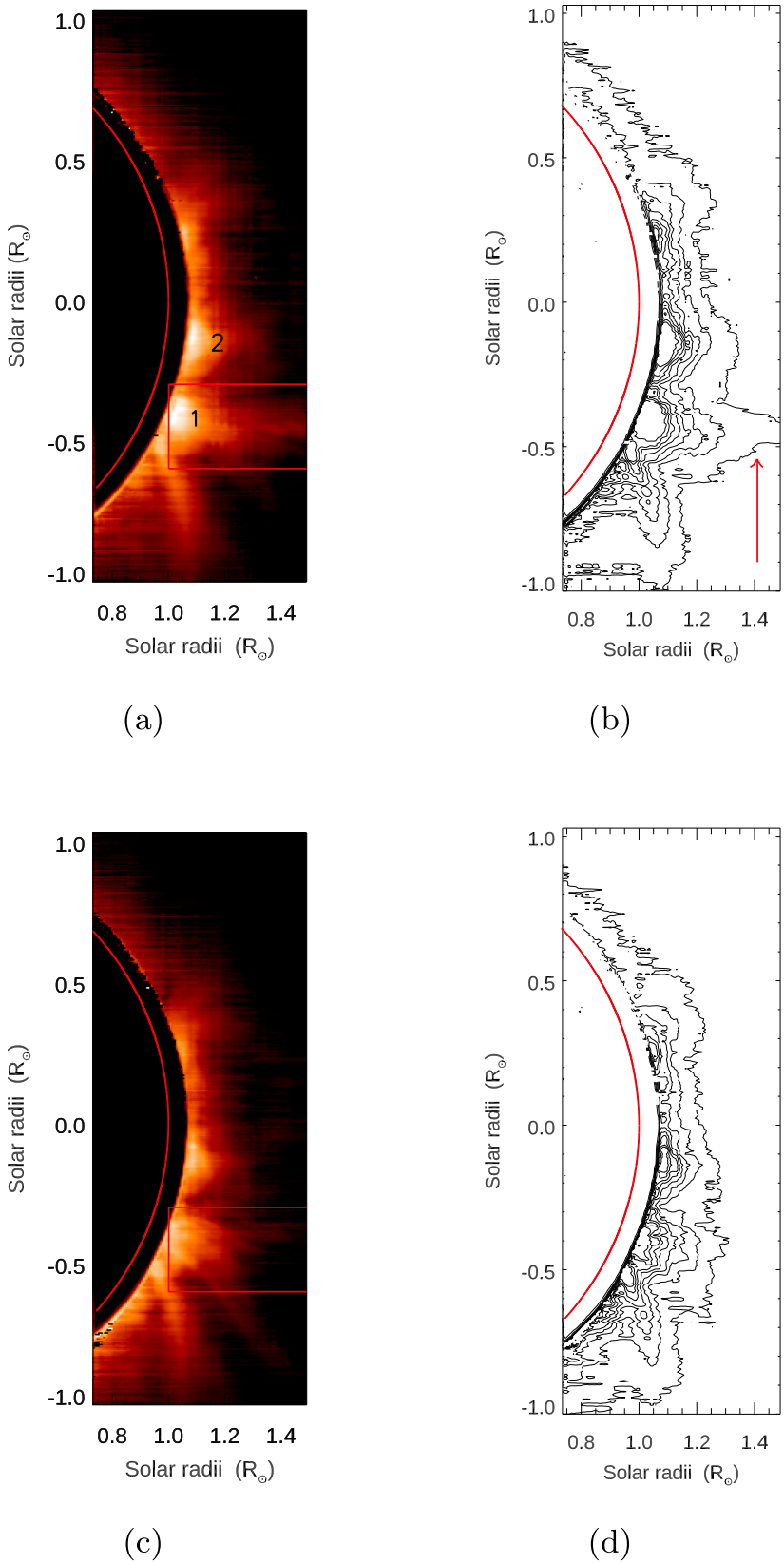

Figure 1. Panel (a): coronal image on the west limb of the Sun in the 5303 Å emission line on 2024 September 13 during the period 00:30–01:05 UT, using raster scan data with VELC. The red arc represents the solar limb ($r = 1R_{\odot}$). The black area with circular edge in the image is the VELC occulter ($r = 1.06R_{\odot}$). Solar north is straight up, and west is to the right. The bright and radially elongated structure seen inside the red box is the CME discussed in the main text. Its position angle (θ), measured in the counterclockwise direction from solar north, is $\approx 270^{\circ}$. The restricted FoV in the north and south directions is due to SNR issues (J. Singh et al. 2025). Numbers 1 and 2 represent the observed enhanced emission due to the CME and activity in the adjacent region, respectively. Panel (b): contour version of the coronal image in (a). The red arrow indicates the bright structure inside the red box in (a). Panel (c): same as (a), but the image period is 01:15–01:50 UT. The structure seen inside the red box has changed and dimmed to a large extent as compared to (a). The coronal region enclosed within the red boxes and the dimensions of the boxes are the same in both cases. Panel (d): contour version of the coronal image in (c). The bright structure and its absence can be noticed more clearly in the contour images in (b) and (d).

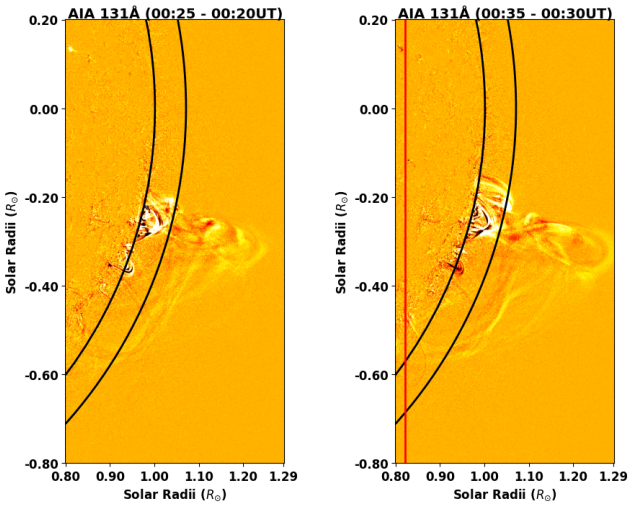

Figure 2. Panel (a): close-up view of the SDO/AIA 131 Å difference image of the Sun near its southwest limb on 2024 September 13. The inner black arc represents the solar limb ($r = 1R_\odot$). The outer black arc indicates the extent of the VELC occulter ($r = 1.06R_\odot$). Panel (b): same as the image in (a) but at later epoch. The vertical red line indicates the VELC raster position at 00:35 UT. The propagating bright emission beyond the VELC occulter in the two images corresponds to the CME discussed in the main text.

in the VELC observations. As per the catalog, the first recorded height–time (h–t) measurement of the leading edge (LE) of the CME is at $r \approx 2.97R_\odot$, around ≈01:36 UT. An inspection of the 131 Å images of the solar corona obtained with the Atmospheric Imaging Assembly (AIA; J. R. Lemen et al. 2012) on board the Solar Dynamics Observatory (SDO) shows that the CME LE is at $r \approx 1.24R_\odot$, close to ≈00:25 UT. The FoV is $\approx 1.29R_\odot$. The LE is near the edge of the FoV at ≈00:35 UT, implying a speed of ≈58 km s^{-1} (Figure 2). These numbers indicate that the CME is present within the FoV of VELC (1.05–$1.5R_\odot$) during the first raster scan period (00:30–01:05 UT). The abovementioned close association between VELC, SDO/AIA, and SOHO/LASCO observations motivated us to investigate the near-Sun characteristics of the CME from the VELC observations.

Figure 3, panels (a)–(e), shows the SDO/AIA 131 Å difference images at multiple epochs during 00:42–00:54 UT, in the VELC first raster scan period mentioned above. The CME is clearly seen in the FoV. Considering the size of the Sun's image on 2024 September 13 from the Sun–Earth Lagrangian L1 location and the occulter size in the VELC, we find that the edge of the occulter will be at $r = 1.06R_\odot$. The coronal locations that are observed with slit 4 of the VELC in the distance range $r = 1.06$–$1.29R_\odot$, at different epochs in the raster scan mode, are indicated in panels (a)–(e). Note that the start time of the VELC first raster scan is 00:30 UT, but the images mentioned above indicate that the CME is present in the FoV of slit 4 only from ≈00:45 UT. The CME LE is near the edge of the SDO/AIA FoV at 00:35 UT, as indicated by Figure 2, panel (b). So, raster observations with the VELC slit 4 in the present case (from 00:45 UT until the end of the first raster scan period at 01:05 UT) correspond to the frontal structure of the CME behind its LE. The coronal locations observed by the VELC slit 4 in panel (f) is same as that in panel (b), but the epoch of observations (01:30 UT) in panel (f) is during the VELC second raster scan period (01:15–01:50 UT). The CME is too faint to be seen in this SDO/AIA image. The VELC second raster scan image is consistent with this (Figure 1, panels (c) and (d)).

Figure 4 (left panel) shows the 5303 Å coronal emission spectrum obtained with the VELC at different epochs and distances during the first raster scan period. The emission relating to the bright regions 1 and 2 in panel (a) of Figure 1 can be seen in each spectrum. The spectral profiles corresponding to the CME-related emission in the left panel (lowermost bright emission, indicated 1) are displayed in the right panel of Figure 4. They are nicely fitted by a single Gaussian (Section 2). There is a gradual decrease in the peak intensity of the line with increasing distance, but the width remains nearly constant. No Doppler-shifted emission beyond the main profile is seen. We verified this by inspecting the residuals of the fits of all the analyzed profiles. The absence of significant Doppler shift could be also due to the fact that the VELC observations correspond the CME structure behind its LE as mentioned in the previous paragraph, in addition to the SNR issue mentioned earlier.

3. Results and Discussions

The solar corona is optically thin. So, the intensity (I) of the observed Fe XIV (5303 Å) emission line is directly proportional to the integrated N_e and emission measure (EM) along the LoS. This property makes the 5303 Å line a useful diagnostic tool for probing the density distribution and thermal properties of the coronal plasma. If the plasma in the emitting volume is isothermal, then $I(\lambda) = G(T, \lambda, N_e) \times \mathrm{EM}$ (E. Landi & M. Landini 1997; E. Landi et al. 2002). $I(\lambda)$ is in units of erg s^{-1} cm^{-2} sr^{-1}. $G(T, \lambda, N_e)$, the contribution function, is calculated using the CHIANTI atomic database.[6] It contains all the relevant atomic physics parameters as a function of T, N_e, and λ, including the elemental abundance Ab, which is assumed to be constant along the LoS.[7] The line intensity (I) has a collisionally excited component due to collisions between ions and electrons and a radiatively excited component due to resonant excitation of ions by light from the solar photosphere. We assumed that collisional excitation dominates the formation of the 5303 Å emission line at $r < 1.2R_\odot$ (M. Waldmeier 1975; K. P. Raju et al. 1991; S. R. Habbal et al. 2011). The distance to which the collisional excitation is important depends on the underlying coronal structures also. For brighter structures like prominences and CMEs, it can be up to comparatively longer distances (S. R. Habbal et al. 2013; B. Boe et al. 2018).

To measure the flux due to the CME, we considered the brightest region in the CME near the occulter edge in the VELC first raster scan image (region 1 in panel (a) of Figure 1). Its half-widths in the lateral and radial directions are ≈75″ and ≈110″, respectively. These values are in good agreement with the size of a CME flux rope structure at $r \approx 1.1R_\odot$ (N. Gopalswamy et al. 2012). The observed peak emission is at $r \approx 1.06R_\odot$. Assuming the LoS depth of the structure to be the same as its radial width (see, e.g., X. Cheng et al. 2012), we estimated the volume (V) of the structure to be $\approx 3.4 \times 10^{29}$ cm^3. This compares well with the near-Sun volume ($\approx 4 \times 10^{29}$ cm^3) of the CME in the study of I. G. Hannah & E. P. Kontar (2013). The observed peak

[6] https://www.chiantidatabase.org/
[7] https://www.chiantidatabase.org/tech_reports/

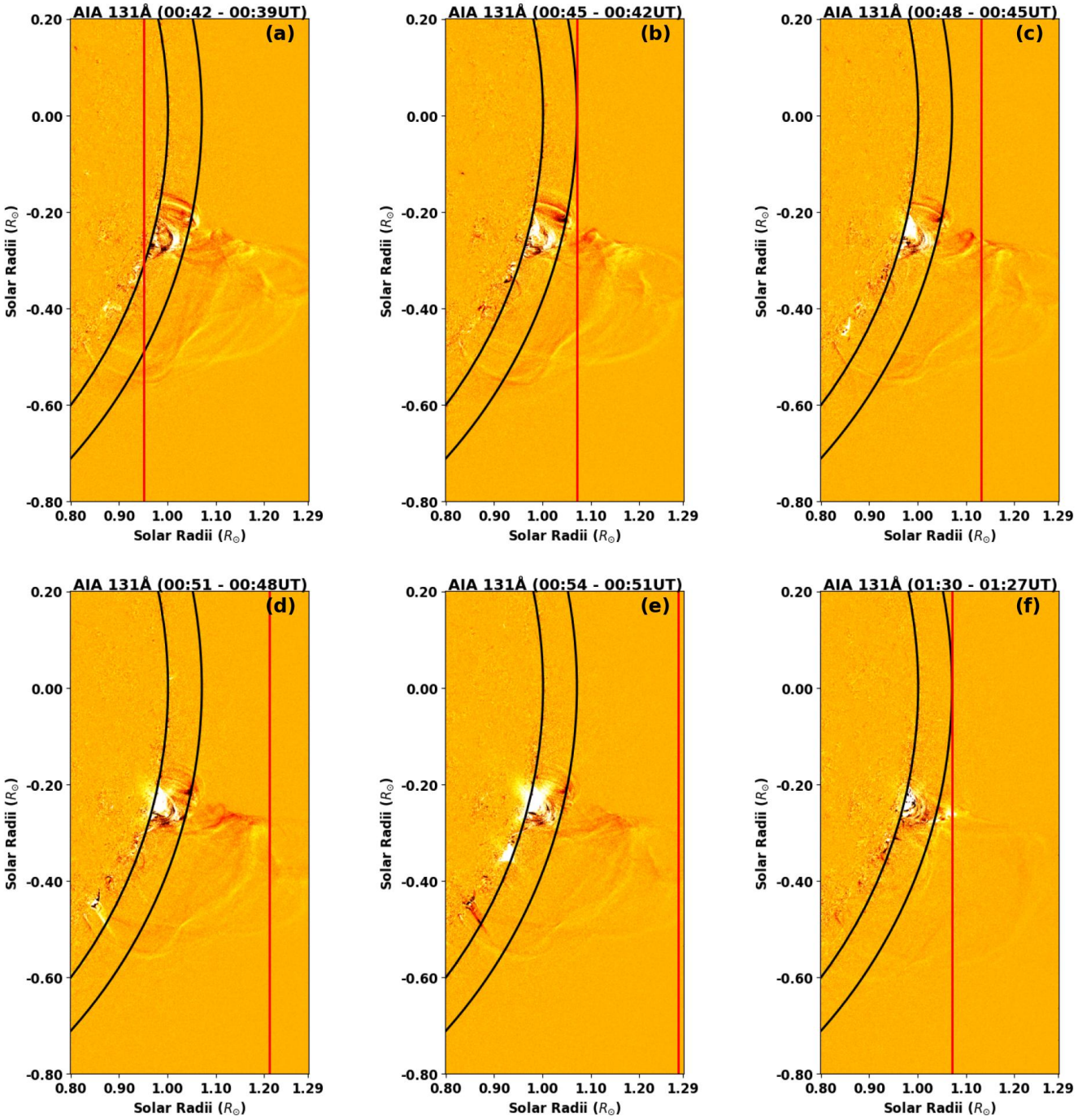

Figure 3. SDO/AIA 131 Å difference images showing the propagation of the CME mentioned in the main text. The inner black arc represents the solar limb ($r = 1R_\odot$). The outer black arc indicates the extent of the VELC occulter ($r = 1.06R_\odot$). The vertical red line in each image indicates the VELC raster position at the epoch of observations, i.e., the latter time indicated in the respective titles. The images in panels (a)–(e) and (f) are during the VELC first and second raster scan periods, respectively.

detector count at the abovementioned location ($r \approx 1.06R_\odot$) is estimated, before and after the CME (i.e., from the first and second VELC raster scan data, respectively), and converted into flux units following the method described in J. Singh et al. (2025). The flux values are $\approx 45 \pm 0.5$ erg s^{-1} cm^{-2} sr^{-1} and $\approx 26 \pm 0.5$ erg s^{-1} cm^{-2} sr^{-1}, respectively. This implies that enhanced flux due to the CME is ≈ 19 erg s^{-1} cm^{-2} sr^{-1}. The above flux values are consistent with the published reports for the 5303 Å coronal emission line at $r \approx 1.1R_\odot$ (T. Tsubaki 1975; J. M. Pasachoff et al. 2009; J. Singh et al. 2019).

Eclipse observations of the post-CME corona in the 5303 Å emission line indicate that the maximum temperature change close to the Sun is ≈5% of the peak formation temperature (B. Boe et al. 2020). For $T \approx 1.8 \times 10^6$ K (formation temperature of the 5303 Å coronal emission line), the above change corresponds to $\Delta \log T \approx 0.02$. Reports indicate that

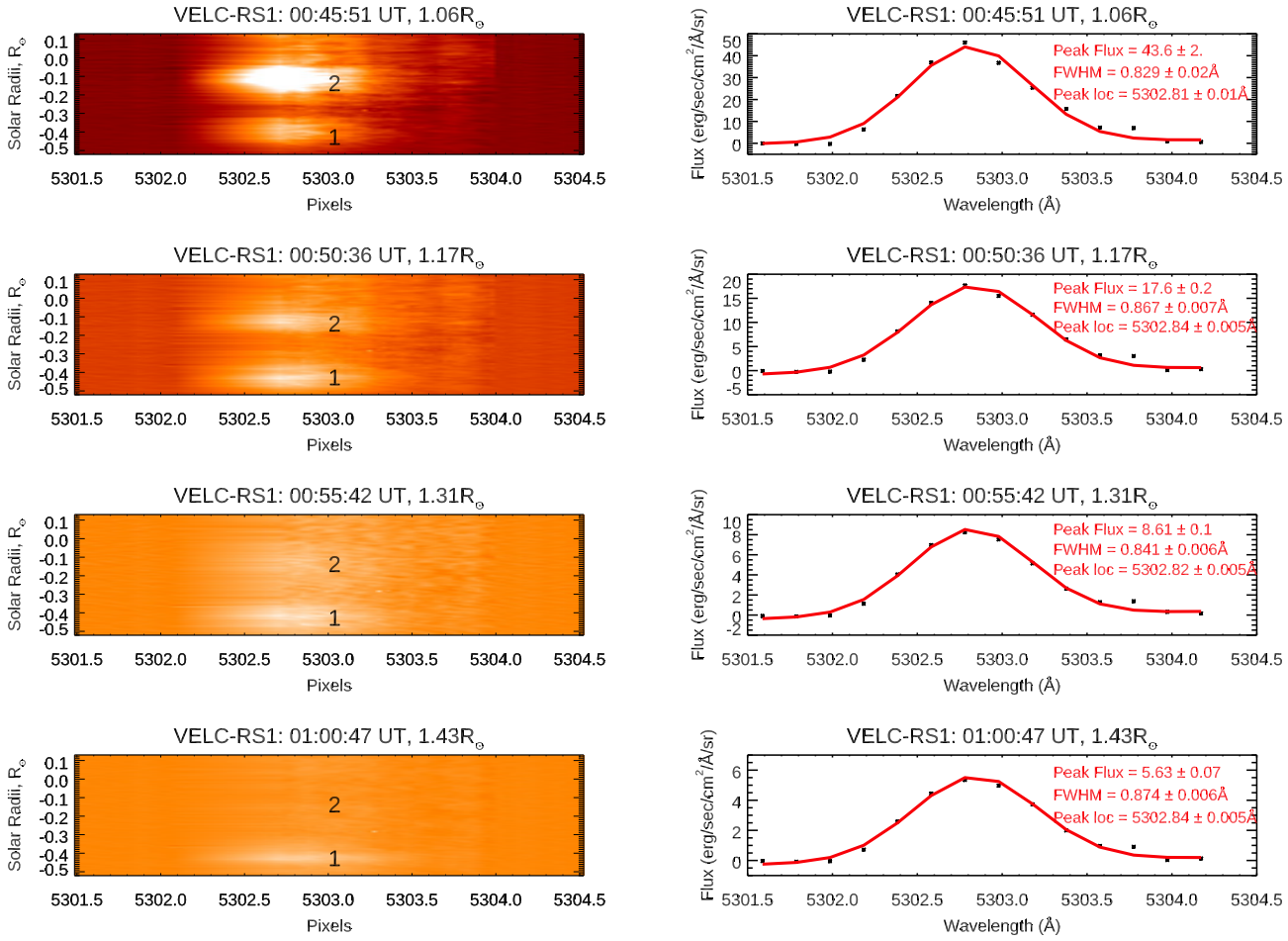

Figure 4. Left panel: 5303 Å emission spectrum related to the observations in Figure 1, at different epochs and distances. The lower most bright emission, indicated 1 in each spectrum, corresponds to the CME shown inside the red box in Figure 1. The brighter emission indicated 2 corresponds to the coronal structure indicated by the same number in Figure 1. Its intensity has decreased more rapidly (compared to the CME associated emission 1) that it is absent in the spectrum obtained around ≈01:00 UT at $r = 1.43R_{\odot}$ (lower left panel). Note that different color scales are used in each of the four spectra to show the emission features with good contrast. Right panel: Spectral profiles corresponding to the bright emission indicated 1 in each spectrum shown in the left panel. The data points in the profiles are flux values in every 7th pixel of the corresponding spectra. The peak emission flux and line width at each epoch and distance are mentioned.

coronal plasma are isothermal for thermal widths up to $\Delta \log T \approx 0.07$ (E. Landi & J. A. Klimchuk 2010). Recent results from the case study of a CME indicates that its expansion in the range $r = 1.05$–$1.35R_{\odot}$ behaves more like an isothermal process (J. Sheoran et al. 2023), similar to the interplanetary CMEs (Y. Liu et al. 2006). Considering the above results, and since differential emission measure (DEM) analysis is ruled out in the present case, we use the simplifying assumption that the CME plasma is isothermal (see, e.g., G. Del Zanna 2013). Assuming $N_e = 10^8\,\mathrm{cm}^{-3}$ for the "background" corona at $r \approx 1.06R_{\odot}$ (G. Del Zanna & E. E. DeLuca 2018), we estimated $G(T,\ \lambda,\ N_e) = 1.7 \times 10^{-26}\,\mathrm{erg\,s^{-1}\,cm^{-3}\,sr^{-1}}$ for $T = 1.8 \times 10^6\,\mathrm{K}$ and $\lambda = 5303\,\text{Å}$. Using the enhanced flux due to the CME mentioned in the previous paragraph for $I(\lambda)$, we then calculated $\mathrm{EM} = I(\lambda)/G(T,\ \lambda,\ N_e) = 1.1 \times 10^{27}\,\mathrm{cm}^{-5}$. This value is an upper limit at the above temperature since the observations are in a single emission line (G. Del Zanna 2013). Nevertheless, it agrees reasonably with the total EM for the CMEs mentioned in other studies (see, e.g., X. Cheng et al. 2012). Based on the analysis of Hinode/XRT data obtained in multiple filters, M. Siarkowski et al. (2008) found that the EM value obtained via isothermal assumption is close to the main peak in the DEM distribution. Markov Chain Monte Carlo simulations for the VELC spectral channels reported by R. Patel et al. (2021) indicate that the observed intensity is maximum, close to the line formation temperature for the individual channels. The above results strengthen our estimates of EM based on isothermal assumption.

The electron density in the CME is calculated using the relation $N_e = (\mathrm{EM}/L)^{0.5}$, where L is the LoS depth (B. R. Dennis & K. J. H. Phillips 2024). Substituting $\mathrm{L} = 110'' = 8 \times 10^9\,\mathrm{cm}$, we estimated N_e to be $\approx 3.7 \times 10^8\,\mathrm{cm}^{-3}$. B. Fort et al. (1973) showed that most of the coronal material is in the green line structures. The authors reported densities $\approx 2 \times 10^9\,\mathrm{cm}^{-3}$ at $r \approx 1.1R_{\odot}$ in quiescent active regions. Similar estimates by H. E. Mason (1975) are in the range 3–$6 \times 10^8\,\mathrm{cm}^{-3}$. Considering the above, the estimate of $N_e \approx 3.7 \times 10^8\,\mathrm{cm}^{-3}$ for the CME in the present case at $r \approx 1.06R_{\odot}$ is reasonable. The thermal energy of the CME is $E_{\mathrm{CME}} = 3N_e k_{\mathrm{B}} TV$, and the mass $M_{\mathrm{CME}} = 1.3 m_p N_e V$ (Q. Zhang et al. 2023). The factor 1.3 accounts for the helium abundance in the solar corona, and $m_p \approx 1.67 \times 10^{-24}\,\mathrm{g}$ is the proton mass. Substituting the different values, we find that $E_{\mathrm{CME}} \approx 9.4 \times 10^{28}\,\mathrm{erg}$ and $M_{\mathrm{CME}} \approx 2.7 \times 10^{14}\,\mathrm{g}$. Closer to the Sun at $1.1R_{\odot}$, the CME thermal energies reported by E. Landi et al. (2010) are in the range 10^{13}–$10^{15}\,\mathrm{erg\,g^{-1}}$. Our estimate in the

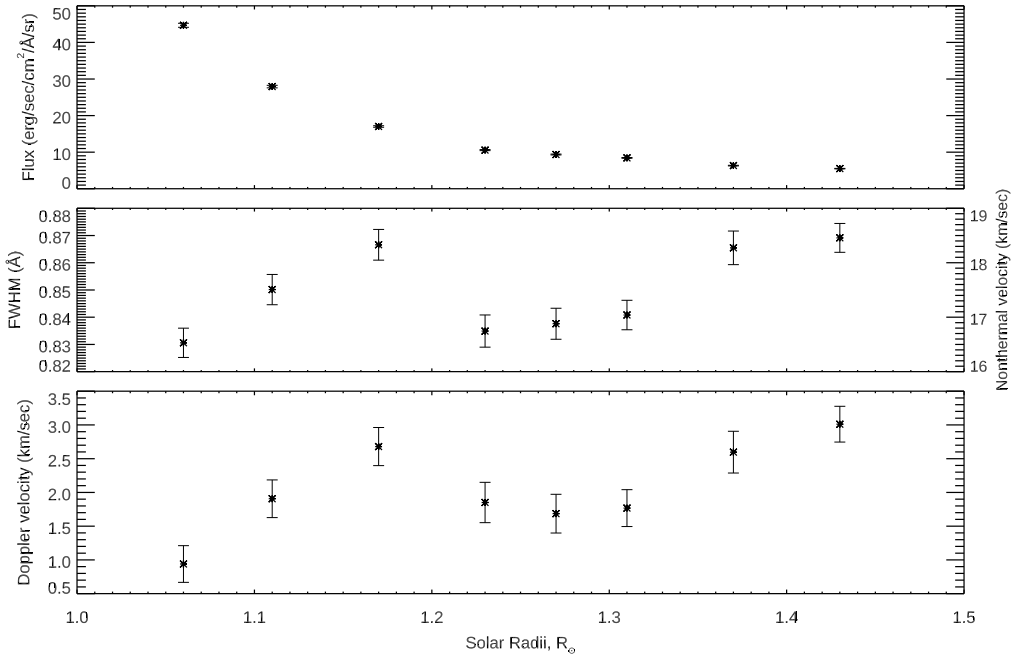

Figure 5. Peak flux, width, and Doppler velocity corresponding to the 5303 Å emission line from the CME in panel (a) of Figure 1, as a function of distance in the VELC FoV. The nonthermal velocity in the line widths is shown in the right-hand-side y-axis for the middle panel.

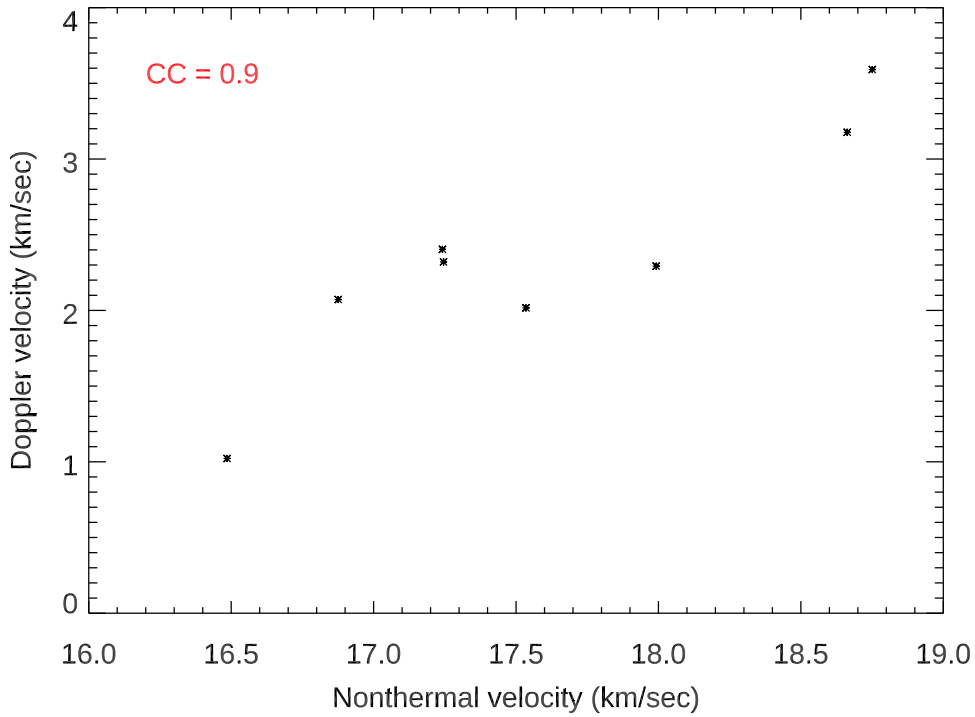

Figure 6. Scatterplot of the nonthermal velocities against the Doppler velocities for the observed 5303 Å emission line from the CME. The correlation coefficient (CC) between the two parameters is 0.9.

present case, 3.5×10^{14} erg g^{-1} at $1.06R_{\odot}$ (obtained by dividing $E_{\rm CME}$ with $M_{\rm CME}$), is consistent with the above result.

It is known from theoretical calculations and total solar eclipse observations that the radiative component in the 5303 Å coronal emission line intensity is nonnegligible even at $r < 1.2R_{\odot}$ (M. Waldmeier 1975; S. R. Habbal et al. 2013; B. Boe et al. 2022; Y. Zhu et al. 2024). Since polarized light in coronal emission lines is associated with radiative (scattering) excitation of anisotropic radiation from the solar disk, R. Casini & P. G. Judge (1999) and others have studied the possibility of measuring coronal magnetic fields using the Zeeman effect and Hanle effect in the 5303 Å line as well as other coronal forbidden lines. Recent calculations using P-CORONA, a new spectral synthesis code to calculate the intensity and polarization of permitted and forbidden coronal lines (H. D. Supriya et al. 2025), indicate that the intensity of 5303 Å line has contribution from radiative excitation at $r \approx 1.02R_{\odot}$ too. Using CHIANTI, we calculated the

contribution of photoexcitation to the line intensity (I) in the present case for $N_e = 3.7 \times 10^8\,\mathrm{cm}^{-3}$, $T = 1.8 \times 10^6\,\mathrm{K}$, $r = 1.06R_\odot$, and 6000 K blackbody radiation temperature. Our calculations show that ≈10% of the observed line intensity is due to radiative excitation. Results reported by M. Waldmeier (1975) and Y. Zhu et al. (2024) indicate that the contribution of photoexcitation at $r \approx 1.06R_\odot$ in the active regions, and N_e as in the present case, is likely to be $\lesssim$15%.

We calculated the peak flux, width, and Doppler velocity of the 5303 Å emission from the CME as a function of distance in the VELC FoV (i.e., ≈1.06–1.50$R_\odot$) also. The average wavelength of the 5303 Å emission line from a large number of high spectral resolution observations with the 25 cm Norikura coronagraph is 5302.8 Å, which corresponds to 5304.3 Å in vacuum (J. Singh et al. 2004, 2006). This wavelength is used as a reference to compute the Doppler velocity. The results of our calculations are shown in Figure 5. There is a gradual decrease in the CME emission flux with distance (upper panel in Figure 5). The line width varies in the range ≈0.83 ± 0.005 Å to ≈0.87 ± 0.005 Å (middle panel in Figure 5), but no unambiguous trend is seen. So, we consider that the line width is nearly constant at ≈0.85 ± 0.02 Å. To note, Y. Zhu et al. (2024) had reported relatively constant line widths in the closed-field regions and same distance range. The nonthermal velocities in the line widths, calculated assuming $T \approx 1.8 \times 10^6$ K for the thermal component of the line width, are in the range 16–19 $\mathrm{km\,s}^{-1}$ (right-hand-side axis in the middle panel of Figure 5). Similar to the line width, the Doppler velocity also indicates a constant redshift at ≈2 ± 1 $\mathrm{km\,s}^{-1}$. Though there are changes, it is difficult to establish a definitive trend (lower panel in Figure 5). We would like to add here that variations in the line width and Doppler velocity, as mentioned above, are not uncommon in the equatorial region beyond the solar limb (L. Contesse et al. 2004). A closer look at the fluctuations in the nonthermal and Doppler velocities indicates ≈90% correlation between them (Figure 6). This strong correspondence suggests unresolved plasma flows and/or turbulence along the LoS could be responsible for the observed excess line widths beyond the thermal broadening (R. O. Milligan 2011).

4. Summary

We have used VELC raster scan spectroscopic observations in the 5303 Å coronal emission line to estimate the near-Sun characteristics of CMEs, like their density, thermal energy, and mass. Utilizing successive raster scan observations on 2024 September 13, before and after the onset of a CME, we estimated the abovementioned parameters at $r \approx 1.06R_\odot$. The corresponding values are $N_e \approx 3.7 \times 10^8\,\mathrm{cm}^{-3}$, $E_{\mathrm{CME}} \approx 9.4 \times 10^{28}$ erg, and $M_{\mathrm{CME}} \approx 2.7 \times 10^{14}$ g, respectively. Though the above values have been derived using observations in a single spectral line, the close correspondence with similar estimates for the CMEs obtained from other observations, particularly in multiple spectral lines, is encouraging. We calculated the widths and Doppler velocities of the line also in the VELC FoV. Both of them are nearly constant at ≈0.85 ± 0.02 Å and ≈2 ± 1 $\mathrm{km\,s}^{-1}$, respectively. The 5303 Å line remains optically thin under typical coronal conditions. So, the observed intensity variations primarily reflect changes in electron density and temperature, providing a reliable method to study the physical properties of the CMEs. With VELC having the capability to observe continuously, and also obtain raster scan images of the solar corona covering an FoV of $\pm 1.5R_\odot$ every ≈20 minutes, the present work indicates a possibility to study the CMEs near the Sun in the visible wavelength range. Joint observations with VELC, UCoMP, and ASPIICS/PROBA-3 in the future can effectively complement each other in such studies. Ground-based multi-site observations during the total solar eclipses are another valuable tool to understand the near-Sun corona.

Acknowledgments

We thank P. Savarimuthu, E. Yuvashree, and S. Nagashree for their help in processing the VELC data. The VELC team members who developed the payload are thanked for their efforts. ADITYA-L1 is an observatory class mission, funded and operated by the Indian Space Research Organization (ISRO). Data obtained with the different payloads on board ADITYA-L1 are archived at the Indian Space Science Data Centre (ISSDC) of ISRO. The CME catalog used is generated and maintained at the CDAW Data Center by NASA and The Catholic University of America in cooperation with the Naval Research Laboratory. SOHO is a project of international cooperation between ESA and NASA. We acknowledge the SDO/AIA team for providing open data access. CHIANTI is a collaborative project involving the University of Cambridge (UK), the NASA Goddard Space Flight Center (USA), the George Mason University (GMU, USA), and the University of Michigan (USA). We are thankful to the referee for kind comments that helped us to present our results more clearly.

ORCID iDs

V. Muthu Priyal https://orcid.org/0000-0001-6093-3302
R. Ramesh https://orcid.org/0000-0003-2651-0204
Jagdev Singh https://orcid.org/0000-0003-0562-2979
K. Sasikumar Raja https://orcid.org/0000-0002-1192-1804

References

Akmal, A., Raymond, J. C., Vourlidas, A., et al. 2001, ApJ, 553, 922
Bemporad, A. 2022, Symm, 14, 468
Bemporad, A., Pagano, P., Giordano, S., & Fineschi, S. 2017, ExA, 44, 83
Bemporad, A., Raymond, J. C., Poletto, G., & Romoli, M. 2007, ApJ, 655, 576
Boe, B., Habbal, S. R., Downs, C., & Druckmüller, M. 2022, ApJ, 935, 173
Boe, B., Habbal, S. R., Druckmüller, M., et al. 2018, ApJ, 859, 155
Boe, B., Habbal, S. R., Druckmüller, M., et al. 2020, ApJ, 888, 100
Brueckner, G. E., Howard, R. A., Koomen, M. J., et al. 1995, SoPh, 162, 357
Casini, R., & Judge, P. G. 1999, ApJ, 522, 524
Cheng, X., Zhang, J., Saar, S. H., & Ding, M. D. 2012, ApJ, 761, 62
Ciaravella, A., Raymond, J. C., Reale, F., Strachan, L., & Peres, G. 2001, ApJ, 557, 351
Contesse, L., Koutchmy, S., & Viladrich, C. 2004, AnGeo, 22, 3055
Del Zanna, G. 2013, A&A, 558, A73
Del Zanna, G., & DeLuca, E. E. 2018, ApJ, 852, 52
Dennis, B. R., & Phillips, K. J. H. 2024, SoPh, 299, 48
Emslie, A. G., Dennis, B. R., Holman, G. D., & Hudson, H. S. 2005, JGR, 110, A11103
Fort, B., Picat, J. P., Dantel, M., & Leroy, J. L. 1973, A&A, 24, 267
Gopalswamy, N., Nitta, N., Akiyama, S., Mäkelä, P., & Yashiro, S. 2012, ApJ, 744, 72
Habbal, S. R., Druckmüller, M., Morgan, H., et al. 2011, ApJ, 734, 120
Habbal, S. R., Morgan, H., Druckmüller, M., et al. 2013, SoPh, 285, 9
Hannah, I. G., & Kontar, E. P. 2013, A&A, 553, A10
Hundhausen, A. J., Gilbert, H. E., & Bame, S. J. 1968, JGR, 73, 5485
Kohl, J. L., Esser, R., Gardner, L. D., et al. 1995, SoPh, 162, 333
Kumar, A., & Rust, D. M. 1996, JGR, 101, 15667
Landi, E., Feldman, U., & Dere, K. P. 2002, ApJ, 574, 495
Landi, E., Gruesbeck, J. R., Lepri, S. T., & Zurbuchen, T. H. 2012, ApJ, 750, 159

Landi, E., & Klimchuk, J. A. 2010, ApJ, 723, 320
Landi, E., & Landini, M. 1997, A&A, 327, 1230
Landi, E., Raymond, J. C., Miralles, M. P., & Hara, H. 2010, ApJ, 711, 75
Lee, J.-Y., Raymond, J. C., Ko, Y.-K., & Kim, K.-S. 2009, ApJ, 692, 1271
Lemen, J. R., Title, A. M., Akin, D. J., et al. 2012, SoPh, 275, 17
Liu, Y., Richardson, J. D., & Belcher, J. W. 2006, P&SS, 53, 3
Mancuso, S., Raymond, J. C., Kohl, J. L., et al. 2002, A&A, 383, 267
Mason, H. E. 1975, MNRAS, 171, 119
Milligan, R. O. 2011, ApJ, 740, 70
Murphy, N. A., Raymond, J. C., & Korreck, K. E. 2011, ApJ, 735, 17
Muthu Priyal, V., Ramesh, R., Singh, J., & Sasikumar Raja, K. 2025, ApJ, 983, 171
Muthu Priyal, V., Singh, J., Prasad, B. R., et al. 2024, AdSpR, 74, 547
Pasachoff, J. M., Rušin, V., Druckmüller, M., et al. 2009, ApJ, 702, 1297
Patel, R., Megha, A., Shrivastav, A. K., et al. 2021, FrASS, 8, 88
Raju, K. P., Desai, J. N., Chandrasekhar, T., & Ashok, N. M. 1991, JApA, 12, 311
Ramesh, R., Muthu Priyal, V., Singh, J., et al. 2024, ApJL, 976, L6
Sheoran, J., Pant, V., Patel, R., & Banerjee, D. 2023, FrASS, 10, 27
Siarkowski, M., Falewicz, R., Kepa, A., & Rudawy, P. 2008, AnGeo, 26, 2999
Singh, J., Prasad, B. R., Suresh Venkata, N., & Amit Kumar 2019, AdSpR, 64, 1455
Singh, J., Ramesh, R., Prasad, B. R., et al. 2025, SoPh, 300, 66
Singh, J., Sakurai, T., & Ichimoto, K. 2006, ApJ, 639, 475
Singh, J., Sakurai, T., Ichimoto, K., & Watanabe, T. 2004, ApJL, 617, L81
Subramanian, P., & Vourlidas, A. 2007, A&A, 467, 685
Supriya, H. D., de Vicente, A., del Pino Alemán, T., Trujillo Bueno, J., & Shchukina, N. G. 2025, ApJ, 987, 39
Tian, H., Tomczyk, S., McIntosh, S. W., et al. 2013, SoPh, 288, 637
Tsubaki, T. 1975, SoPh, 43, 147
Vourlidas, A., Subramanian, P., Dere, K. P., & Howard, R. A. 2000, ApJ, 534, 456
Waldmeier, M. 1975, SoPh, 45, 147
Zhang, Q., Teng, W., Li, D., Dai, J., & Zhang, Y. 2023, ApJ, 958, 85
Zhu, Y., Habbal, S. R., Ding, A., et al. 2024, ApJ, 966, 122